

# Surface and sub-surface reactions during low temperature aluminium oxide atomic layer deposition on fiber-forming polymers

Joseph C. Spagnola,<sup>b</sup> Bo Gong,<sup>a</sup> Sara A. Arvidson,<sup>a</sup> Jesse S. Jur,<sup>a</sup> Saad A. Khan<sup>a</sup> and Gregory N. Parsons<sup>\*ab</sup>

Received 9th February 2010, Accepted 29th March 2010

First published as an Advance Article on the web 19th April 2010

DOI: 10.1039/c0jm00355g

Fundamental reaction processes between vapor-phase chemical precursors and high molecular weight polymers are important for polymer coating, encapsulation and surface modification. Using trimethylaluminium and water in an atomic layer deposition (ALD) exposure sequence, reactions between vapor-phase trimethylaluminium and common polymers with different substituents are quantified using *in situ* infrared transmission analysis. Exposing polypropylene to trimethylaluminium results in reactant uptake with minimal precursor/polymer reaction, but the precursor/water ALD sequence leads to subsurface alumina nucleation. A similar treatment to polyvinyl alcohol and polyamide-6 results in rapid precursor diffusion and significant reaction observed by IR, and the extent of reaction is consistent with results from *in situ* quartz crystal microgravimetry and transmission electron microscopy. Reacting trimethylaluminium with polyamide-6 leads to methyl group insertion into the amide carbonyl group and interaction with the hydrogen-bonded amine units. Multiple ALD reaction cycles produce film coatings on all polymers studied, but the coating structure depends strongly on the starting polymer composition. For the weakly interacting polypropylene, cross-sectional transmission electron microscopy demonstrates enhanced sub-surface growth at 90 °C as compared to that at 60 °C, while images of coated polyamide-6 fibers showed that growth is not strongly temperature dependent in that range. Micrograph images of polyamide-6 samples exposed to extended TMA doses revealed significant modification of the fiber surface region, demonstrating that the precursor could diffuse and react to depths in excess of 100 nm into the surface of the polymer at 90 °C. Improved understanding of specific precursor/polymer reaction pathways can be important to optimize the performance of conformal inorganic thin film coatings on polymers.

## I. Introduction

Specialized applications of organic polymer film and fiber materials are expanding the need for well defined and controlled inorganic thin film coatings. A few important applications where inorganic thin film coatings can add function and longevity to polymer films and fibers include passivation and encapsulation layers for organic photovoltaics and light emitting diodes,<sup>1</sup> food and medical packaging barriers,<sup>2</sup> nanofiber coatings for chemical separations and protective systems,<sup>3,4</sup> and surface modification for bioengineering and biocompatibility.<sup>4–6</sup> For many material systems, the function and performance of the inorganic coating depend on the nature of the resulting polymer/inorganic interface. The detailed structure of the interface is determined largely by the chemical or physical process used for inorganic film deposition, as well as the specific chemical interactions between depositing species and the polymer surface or chain.<sup>7–11</sup> While studies addressing properties and performance of thin film inorganic coatings on polymers are widely found, detailed investigations of the chemical reaction mechanisms between the polymer and the vapor-phase deposition species are less

common.<sup>7–11</sup> Understanding the chemical reaction pathways enables the interface to be better defined and controlled. In addition, surface reaction control can also enable direct formation of useful structures. For example, patterns of self-assembled organic monolayers with designed surface termination can spatially define sites to promote<sup>12</sup> or impede<sup>13–15</sup> film nucleation and growth, producing self-patterned films for electronic devices or other pre-determined function.

Plasma processes generate reactive radicals and ions in the gas phase that function to modify or coat polymers, or activate nonreactive surfaces to promote film nucleation.<sup>1,2,16,17</sup> However, plasma-generated radicals and ultraviolet radiation can also act to break down and degrade polymers. Recent interest<sup>18–26</sup> is turning to atomic layer deposition (ALD) for inorganic film growth on polymers because it can produce well defined conformal coatings at low deposition temperatures using thermally driven reactions. Atomic layer deposition involves a binary sequence of self-limiting reactions that produce a highly conformal film with precise thickness control at low deposition temperatures. The conformality and precision of ALD coatings also make the process interesting for coating polymer fibers and fiber mats with high surface area.<sup>27–30</sup>

This study focuses on chemical reactions that occur upon vapor-phase metal-organic precursor exposure during low-temperature atomic layer deposition on reactive and nonreactive polymer surfaces. Several common polymers with different

<sup>a</sup>Department of Chemical and Biomolecular Engineering, North Carolina State University, Raleigh, NC, 27695, USA. E-mail: parsons@ncsu.edu

<sup>b</sup>Department of Materials Science and Engineering, North Carolina State University, Raleigh, NC, 27695, USA

substituents were chosen to quantify distinct reaction mechanisms. Results show, for example, that cast polyamide-6 (PA-6) thin films with reactive amide bonding units, hydrogen bonding between polymer chains, and affinity for water absorption, undergo rapid reaction with trimethylaluminium (TMA) at 90 °C. The mass uptake in polyamide-6 during TMA exposure, measured using *in situ* quartz crystal microgravimetry analysis, is 10× larger than for similar exposures on polyvinyl alcohol (PVA) films containing reactive hydroxyl bonding units. Polypropylene (PP) films lacking reactive functional groups show smaller mass uptake during TMA exposure, similar to that measured during Al<sub>2</sub>O<sub>3</sub> ALD on dense Al<sub>2</sub>O<sub>3</sub> substrates. The mass uptake observed on PP, however, is more sensitive to deposition temperature than the other polymers investigated. *In situ* infrared transmission during the ALD reaction sequence on polymer films and fibers permits chemical mechanisms associated with polymer/precursor interaction to be probed and quantified, and the mechanisms identified are consistent with the mass uptake analysis performed using quartz crystal microbalance.

An improved understanding of initial reactions during vapor phase ALD reaction processing, including more clearly defined conditions for inorganic film nucleation on polymers, is expected to help improve the viability and function of inorganic coatings and surface modification of polymer films and fibers for advanced applications, including control of polymer reactivity, wettability, and chemical affinity and adhesion.

## II. Experimental materials and methods

### Preparation of polymer fibers and films

Melt blown polypropylene ((C<sub>3</sub>H<sub>6</sub>)<sub>n</sub>,  $T_g \approx -10$  °C) nonwoven fiber mats were prepared from Sunoco Chemicals Polymers Division, product CP360H (reported number average molecular weight, M<sub>n</sub> = 58.5 kDa) using a 0.56 meter pilot-scale melt blowing line located in the Nonwoven Cooperative Research Center at NC State University. The PP fibers in the resulting nonwoven mat have diameters between 1 μm and 10 μm, and the overall mat thickness is ~0.3 mm. Polypropylene films were prepared by dissolving 1 wt% PP in decahydronaphthalene (C<sub>10</sub>H<sub>18</sub>, Decalin, cas number: 91-17-8) at 165 °C for 1 hour. Approximately 80 μl of the solution were then dispensed onto a heated substrate and spuncast at 3000 rpm for 1 min to evaporate the solvent. Ellipsometry analysis (Alpha SE, J.A. Woollam) of the spuncast PP films on silicon showed the film thickness to be ~30 nm.

Polyvinyl alcohol ((C<sub>2</sub>H<sub>4</sub>O)<sub>n</sub>,  $T_g \approx 85$  °C) solutions for electrospinning were prepared by mixing 7 wt% PVA resin (Aldrich Chemistry, Mowiol® 40-88, M<sub>n</sub> = 112 kDa) in deionized (DI) water at 60 °C overnight. Prepared solutions were stored at 8 °C until use. The electrospinning apparatus was based on a point-plate configuration and included a precision syringe pump (Harvard Apparatus, Holliston, MA) that operated at a flow rate 0.5 ml h<sup>-1</sup>. The high-voltage power supply (Gamma High Voltage Research, model D-ES30 PN/M692 with a positive polarity) operating voltage was approximately 12 kV at a tip-to-collector distance of 15 cm. The solutions were loaded into 10 ml syringes with luer-lock connections fitted to 2 inch long, 22-gauge blunt tip needles. A continuous random nonwoven fiber mat was

collected on an aluminium foil-covered stainless steel flat collector plate for 400 minutes, resulting in a typical fiber diameter of 250 nm. Polyvinyl alcohol films were prepared by dissolving 2 wt% PVA in DI water. Approximately 80 μl of the solution were then dispensed onto a substrate and spuncast at 2000 rpm for 1 min, resulting in films ~30 nm thick (from ellipsometry).

Polyamide-6 ((C<sub>6</sub>H<sub>11</sub>N)<sub>n</sub>,  $T_g \approx 50$  °C) fibers (typically 10 μm diameter) were used as received from Allaso Industries. Polyamide-6 thin films were produced by dissolving 1 wt% PA-6 (Ultramid(R) B27 02, BASF M<sub>n</sub> ≈ 16 kDa) in formic acid (Fluka Analytical, ~98% purity, 2% H<sub>2</sub>O). Approximately 80 μl of the solution were then dispensed onto a silicon or quartz substrate and spuncast at 6000 rpm for 1 min, also resulting in a film ~30 nm thick.

### Atomic layer deposition reactor and process

Atomic layer deposition of aluminium oxide was performed in a custom hot wall reactor system using sequential exposures to trimethylaluminium (TMA, 98% purity, STREM chemical) and water (UV-deionized). Ultra-high purity argon gas, further purified by an Aeronex gatekeeper inert gas purifier, is used as a reactant carrier gas and to purge the reactor between exposure steps. The reaction chamber consists of a stainless steel tube 1.5 inches in diameter and ~24 inches in length, equipped with external resistive heaters modulated using a temperature controller (Eurotherm, model 808). Precursor and reactant gases are introduced at the end of the tube reactor *via* separate, heated 0.25 inch stainless steel gas lines. The system is brought to vacuum *via* a rotary mechanical pump and pressure is monitored using a convection gauge (Granville-Phillips). The system operates at ~1.5 Torr with a gas flow rate of approximately 200 standard cubic centimetres per minute (sccm). Typical precursor dose and purge times were TMA/Ar/H<sub>2</sub>O/Ar = 1.2/40/1.2/50 seconds, which correspond to a single ALD cycle. One hundred ALD cycles at 60 °C on an oxide-coated silicon substrate produced a film that was 112 Å thick (as determined by ellipsometry), corresponding to a growth rate of ~1.1 Å per cycle.

*In situ* quartz crystal microgravimetry (QCM) was used during ALD to characterize mass changes during reactant exposure steps. Quartz crystals (SC-101, resonant frequency nominally 6 MHz) were obtained from Inficon and used as received. A diagram of showing the QCM arrangement in the flow tube reactor is shown in Fig. 1a. For some experiments, the quartz crystal surface was coated with spuncast polymer film. The QCM crystal was mounted to the sensor head (Maxtek BSH-150) and vacuum sealed into the reaction chamber. The sensor head was modified to allow inert gas purging (~10 sccm) to the backside of the QCM crystal to prevent film deposition near the electrical contacts to the crystal. The QCM sensor head was connected to a crystal thickness monitor (Inficon SQM-160) which allows for computer interface to collect a frequency signal every 0.15 seconds. Particular care was taken to be sure that the temperature of the QCM setup was stable within the reactor. Typically, following the loading of the QCM crystal, the temperature was allowed to equilibrate for several hours (often overnight) before collecting QCM data. Some of the polymer coated QCM crystals occasionally gave intermittent signals,

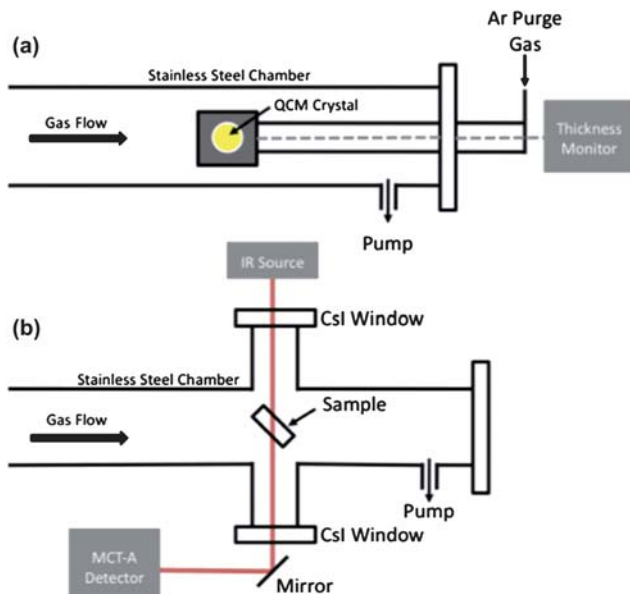


**Fig. 1** Sample arrangement geometries in the tubular ALD reactors during (a) *in situ* QCM and (b) *in situ* transmission FTIR investigations.

especially after exposure to many ALD cycles, due to the challenge of securing good electrical contact to the polymer-coated crystal in the QCM housing and the ability of the ALD coating to penetrate into the contact region on these samples.

The polymer fibers and films were also exposed to ALD reactant species in a separate custom built, viscous flow vacuum reactor equipped with *in situ* transmission FTIR capability. A diagram showing the sample configuration in the FTIR-compatible reactor is shown in Fig. 1b. The reaction system is composed of a stainless steel tube 1.5 inches in diameter with a resistively heated jacket to achieve the desired temperature. A controlled temperature gradient was maintained along the entire gas flow path to prevent precursor condensation. Ultra-high-purity (99.999%) Argon gas was used as the purge and carrier gas after further purification by a gas filter (DRIERITE Gas Purifier). To allow for transmission of the IR beam through the sample, two single crystal CsI IR windows are attached on the sides of the sample area, and two gate valves were installed between the IR window and chamber to prevent deposition on the IR windows. The IR beam produced by a Nicolet 6700 FTIR system enters through the CsI IR window and impinges on the sample. The transmitted beam then exits through the second window and is focused by a gold parabolic mirror into an external mercury–cadmium–telluride detector with type-A sensitivity (MCT-A). In a typical TMA/water deposition cycle, the TMA and H<sub>2</sub>O were allowed to flow for 5 s, followed by 60 seconds of chamber isolation, during which the valve to the pump was closed and gas flow was stopped. This isolation step ensured full reaction saturation on the polymer surface. Argon gas was then allowed to flow for 120 s to purge the reactor before IR measurement. Transmission IR data were collected under static Ar gas pressure of ~7 mTorr. All depositions and spectra collection steps were performed with temperature fixed at 90 °C. As a control, FTIR transmission studies of Al<sub>2</sub>O<sub>3</sub> ALD were performed using anodic aluminium oxide (AAO) membranes

(Anodisc), and these substrates were used as received. High-resistivity polished silicon wafers (Silicon Valley Microelectronics) were used as substrates for FTIR characterization of polymer films. Polymer fibers were also supported on high resistivity silicon wafers for IR measurement.

### Transmission electron microscopy

Cross-sectional transmission electron microscopy (TEM) was used to evaluate the growth of the aluminium oxide on the polypropylene and polyamide-6 fibers. Coated fiber samples were embedded in Spurr low-viscosity epoxy resin (Ladd Research Industries) and allowed to cure overnight at room temperature. The resulting solid blocks were then trimmed and cut using a Lecia Ultracut diamond knife microtome to a thickness of 70 nm. The sections were then floated in water onto 300 mesh grids and allowed to dry. Transmission electron microscopy of coated PVA fibers was not feasible because the fiber material is highly soluble in water and therefore was incompatible with the water-based microtome and focused ion beam sample preparation methods.<sup>31</sup> Attempts to prepare cross-sectional PVA/Al<sub>2</sub>O<sub>3</sub> samples for TEM were not successful. The TEM images of PA-6 and PP coated fibers were obtained using a Hitachi HF-2000 system using a cold field emission electron source with an accelerating voltage of 200 kV. Because of the difference in mechanical response of the epoxy, fiber, and coating, shearing can occur during the microtome process resulting in void formation and thin film cracking which are visible in the resulting TEM images. Cross-sectional samples of Al<sub>2</sub>O<sub>3</sub> coated PP fibers prepared by focused ion beam processing and imaged by SEM (images not shown) did not show cracking in the aluminium oxide films.

## III. Results and discussion

### A. *In situ* analysis of ALD Al<sub>2</sub>O<sub>3</sub> film growth on Al<sub>2</sub>O<sub>3</sub>

To better understand chemical processes during Al<sub>2</sub>O<sub>3</sub> ALD on polymers, we first applied our *in situ* characterization tools to examine Al<sub>2</sub>O<sub>3</sub> ALD on Si and Al<sub>2</sub>O<sub>3</sub> surfaces. Fig. 2a shows the mass uptake measured using *in situ* QCM during sequential exposures to TMA and H<sub>2</sub>O separated by Ar gas purge steps. To prepare the Au-coated quartz crystal surface before data collection, the surface was exposed to more than 100 cycles of Al<sub>2</sub>O<sub>3</sub> ALD (film thickness ≈ 10 nm). Fig. 2a shows the mass uptake in ng cm<sup>-2</sup> plotted versus data collection time for 100 ALD cycles at 60 °C and 90 °C. The mass uptake rate is linear with time and average values of the data points shown in Fig. 2b are  $53.5 \pm 3.5$  ng cm<sup>-2</sup> per cycle at 90 °C, and  $58.6 \pm 5.0$  ng cm<sup>-2</sup> per cycle at 60 °C, consistent with previous reports.<sup>32–34</sup> The uncertainties represent the standard deviation of 100 measured values. The mass uptake is constant through the film growth and nearly the same at the two temperatures studied, with somewhat larger scatter in the data collected at 60 °C.

Fig. 3 shows FTIR differential spectra collected during two ALD Al<sub>2</sub>O<sub>3</sub> cycles at 90 °C on an anodic aluminium oxide membrane substrate. Key features of interest include the broad Al–OH mode between 3750 cm<sup>-1</sup> and 2900 cm<sup>-1</sup> and the methyl stretching bands at 2930 cm<sup>-1</sup>, 2900 cm<sup>-1</sup>, and 2830 cm<sup>-1</sup>. Features near 1660 cm<sup>-1</sup> and 1210 cm<sup>-1</sup> correspond to bending

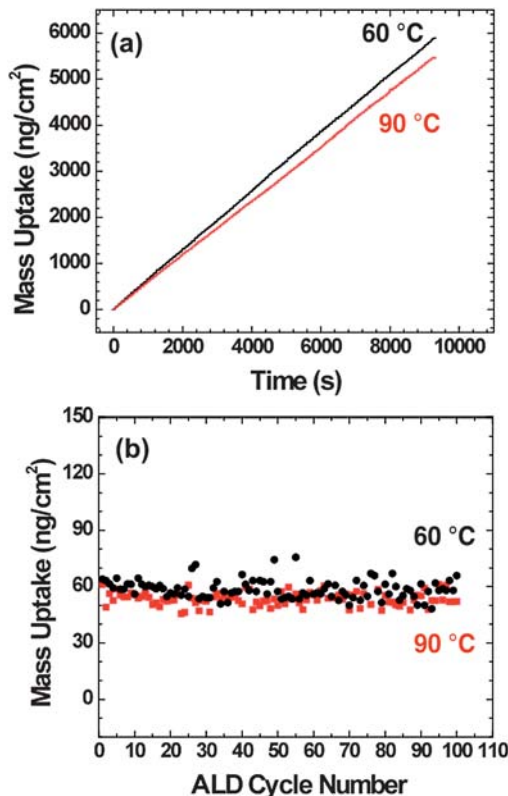


**Fig. 2** *In situ* Quartz crystal microgravimetry during ALD of Al<sub>2</sub>O<sub>3</sub> at 90 °C. Panel a shows linear film growth rates throughout 100 ALD cycles at 60 °C and 90 °C. Panel b shows the mass uptake for each ALD cycle for 100 cycles at 60 °C and 90 °C.

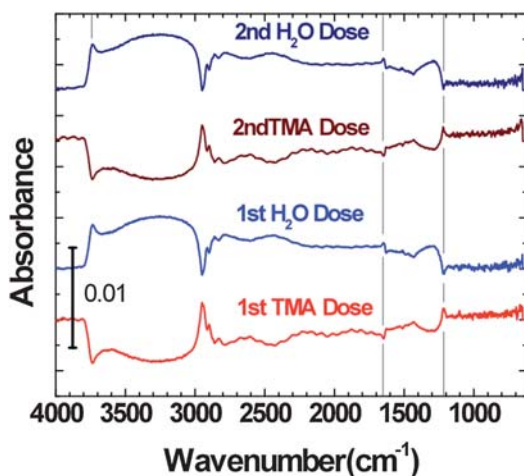


**Fig. 3** *In situ* differential FTIR spectra collected during two cycles of Al<sub>2</sub>O<sub>3</sub> ALD on an anodic aluminium oxide disk at 90 °C. Features of interest include: OH stretching (3750 and 2830 cm<sup>-1</sup>), CH<sub>3</sub> stretch (2930, 2900, 2830 cm<sup>-1</sup>), OH bending (1660 cm<sup>-1</sup>), CH bending (1210 cm<sup>-1</sup>), CH<sub>3</sub> bending (1190 cm<sup>-1</sup>), and CH<sub>3</sub> rocking (690 cm<sup>-1</sup>). Alternating surface chemistry of methyl groups after TMA doses and hydroxyl groups after water doses is readily observed.

modes of surface physisorbed water molecules<sup>35</sup> and C–H bending modes, respectively. When the Al<sub>2</sub>O<sub>3</sub> growth surface was exposed to TMA, the Al–OH absorbance decreased, and the methyl band intensity increased. A decrease in the water mode

and an increase in the methyl bending feature are also noted. During the subsequent water dose, hydroxyl bands increased and C–H modes decreased in intensity, consistent with expected ALD surface reaction sequence.<sup>35,36</sup>

### B. *In situ* mass uptake analysis on polymer films

For several experiments, QCM crystals were spin-coated with a polymer film and initial mass uptake was measured on the untreated polymer under the same deposition conditions used for the data in Fig. 2. Fig. 4a shows the resulting mass uptake in ng cm<sup>-2</sup> plotted *versus* time during the first 5 Al<sub>2</sub>O<sub>3</sub> ALD cycles on a QCM crystal coated with ~30 nm of PVA and PP. The data from Fig. 2 for mass uptake on an Al<sub>2</sub>O<sub>3</sub> coated crystal are also reproduced at higher resolution in Fig. 4a as a reference. The mass uptake during the TMA exposure step on PVA is significantly larger than that measured for the same exposures on Al<sub>2</sub>O<sub>3</sub> or virgin PP surfaces. Several mass uptake experiments were performed using different thicknesses of PVA coatings on the QCM crystal. A PVA layer ~5 nm thick showed less mass uptake whereas a ~15 nm PVA film showed mass uptake similar to the data for the ~30 nm film shown in Fig. 4a. This result indicates that the ~30 nm PVA film was sufficiently thick that the TMA uptake during the 1.2 second exposure did not saturate the film. Fig. 4b shows mass uptake results recorded using a QCM crystal coated with ~30 nm of PA-6 alongside the control data for ALD on Al<sub>2</sub>O<sub>3</sub>. The PA-6 shows a much larger mass gain during the first ALD cycle than for deposition on Al<sub>2</sub>O<sub>3</sub> or on PVA.

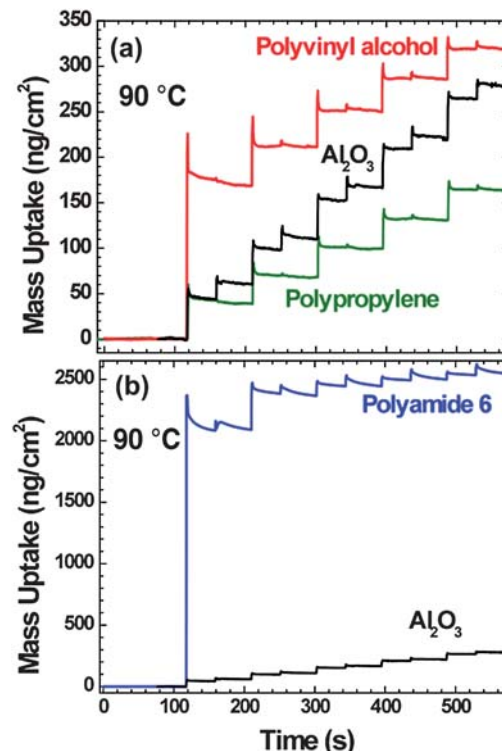


**Fig. 4** *In situ* Quartz crystal microgravimetry during the first 5 ALD cycles of Al<sub>2</sub>O<sub>3</sub> on QCM crystals coated with polymer. Panel a shows PVA, and PP with Al<sub>2</sub>O<sub>3</sub> shown as a reference. Panel b shows PA-6, with Al<sub>2</sub>O<sub>3</sub> shown as a reference. Both the PVA and PA-6 show enhanced mass uptake during the first ALD cycle.

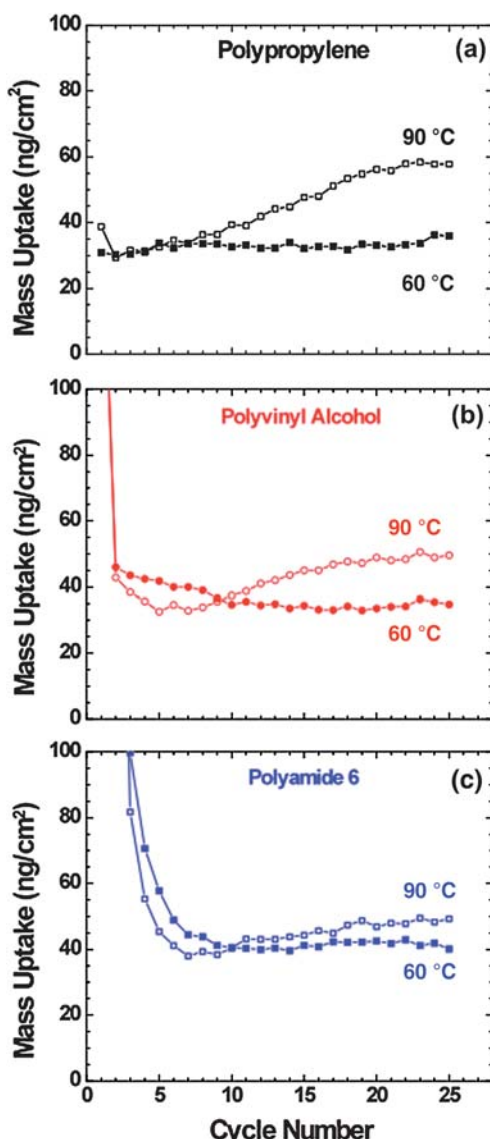
The mass gain during each TMA exposure cycle on PP, PVA, and PA-6 was recorded over the initial 25 ALD cycles at 60 °C and 90 °C, and results are shown in Fig. 5a–c for deposition on PP, PVA, and PA-6 respectively. Over the initial 25 cycles on PP at 60 °C, the mass gain per ALD cycle remains nearly constant at 35 ng cm<sup>-2</sup> per cycle, whereas at 90 °C the mass gain increases to 62 ng cm<sup>-2</sup> per cycle by the 25<sup>th</sup> cycle. This trend is ascribed to TMA diffusion and reaction with water in the near-surface region of the PP during the early growth cycles, followed by increased mass uptake during subsequent cycles as aluminium oxide deposits onto surface and subsurface aluminium oxide nuclei. The growth on PVA in Fig. 5b demonstrates a large mass uptake during the first ALD cycle, followed by a nearly constant mass uptake. Some enhanced mass uptake is also observed at

90 °C versus 60 °C on PVA, similar to the trend observed on PP. Data in Fig. 5c show that the large mass uptake on PA-6 proceeds over the first 5 cycles at both 60 and 90 °C, then continues nearly independent of temperature.

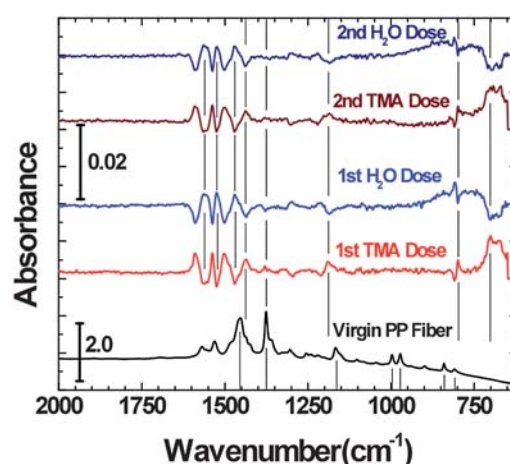
### C. *In situ* FTIR analysis of precursor–polymer interaction

Fig. 6 shows *in situ* FTIR differential absorbance spectra collected during two ALD aluminium oxide cycles on nonwoven melt-blown PP fibers at 90 °C. A reference absorbance spectrum of the virgin PP fibers is also shown, and absorbance scales are included for the substrate and difference spectra. A nonwoven fiber mat presents a useful surface for direct IR transmission analysis of conformal ALD growth because the surface area of the fiber mat is larger than a planar cast or spin-coated film, and the density of the nonwoven mat can be readily adjusted.<sup>5</sup> Vibrational modes<sup>37</sup> associated with polypropylene include –CH<sub>2</sub> scissors at 1452 cm<sup>-1</sup>, –CH<sub>3</sub> deformation at 1375 cm<sup>-1</sup>, C–C stretching + –CH<sub>3</sub> rocking + C–H bend at 1166 cm<sup>-1</sup>, and –CH<sub>3</sub> rocking + CH bending at 997 cm<sup>-1</sup>, –CH<sub>3</sub> rocking + C–C stretching at 971 cm<sup>-1</sup>, and CH<sub>2</sub> rocking near 841 and 810 cm<sup>-1</sup>. Modes near 1550 and 1640 cm<sup>-1</sup> are ascribed to some oxidation of the polypropylene backbone resulting in blue shift of the C–H scissors deformation and combination modes. This is also consistent with weak features near 1200 cm<sup>-1</sup> associated with C–O stretching.

After exposing the fiber mat to TMA during the first ALD cycle, changes in the spectrum are observed. Note that the signal for the difference spectra is multiplied by a factor of 100 compared to the starting fiber spectrum. The CH<sub>3</sub> mode at 1375 cm<sup>-1</sup> shows a small increase, and new modes appear at 1437 cm<sup>-1</sup>, 1190 cm<sup>-1</sup>, and 706 cm<sup>-1</sup>. Vibrational data from TMA adsorbed on Si(100) indicate that these modes are due to



**Fig. 5** Mass uptake (ng cm<sup>-2</sup>) per ALD cycle measured by *in situ* Quartz crystal microgravimetry during 25 ALD cycles of Al<sub>2</sub>O<sub>3</sub> at 60 °C and 90 °C on QCM crystals coated with 30 nm of PP (panel a), PVA (panel b), and PA-6 (panel c). Polypropylene shows the largest temperature sensitivity, polyvinyl alcohol shows a moderate sensitivity, and polyamide-6 is relatively insensitive.



**Fig. 6** Absorbance spectrum for untreated polypropylene melt blown fibers, and *in situ* differential FTIR spectra collected during the first two cycles of Al<sub>2</sub>O<sub>3</sub> ALD at 90 °C. Features of interest include: –CH<sub>3</sub> bending (1437 cm<sup>-1</sup>), –CH<sub>3</sub> bending and –CH<sub>2</sub> wagging (1375 cm<sup>-1</sup>), C–C stretching and –CH<sub>3</sub> bending (1190 cm<sup>-1</sup>), and CH<sub>3</sub> rocking (971 cm<sup>-1</sup>). Note the absorbance scale for the differential spectra is magnified by a factor of ~100× compared to that for the fibers. Alternating shifts of the methyl bands in the differential spectra indicate TMA absorption into the polymer.

$\text{CH}_3$  rocking and  $\text{CH}_3$  symmetric and asymmetric deformation, respectively,<sup>38</sup> and are consistent with TMA present on or within the polymer fiber structure. The most noticeable change upon TMA exposure is the oscillatory shape in the difference spectra between 1450 and 1600  $\text{cm}^{-1}$ . We ascribe these features to a shift of  $\text{CH}_2$  bending modes that occur when TMA penetrates into the polymer network. In this process, the electrophilic TMA induces a polarization that strengthens the C–H bonds resulting in a blue shift. The  $\text{CH}_2$  rocking modes near 800  $\text{cm}^{-1}$  undergo similar changes upon TMA exposure. After water exposure, the Al– $\text{CH}_3$  features at 1437  $\text{cm}^{-1}$ , 1190  $\text{cm}^{-1}$ , and 706  $\text{cm}^{-1}$  decrease in intensity, and the changes between 1450 and 1600  $\text{cm}^{-1}$  and near 800  $\text{cm}^{-1}$  indicate a reversal in the mode shifts observed in the previous TMA exposure step. Similar intensity oscillations are observed in Fig. 6 after the second TMA and water exposure cycles. Ferguson *et al.*<sup>18</sup> observed similar oscillatory shifts in  $\text{CH}_2$  modes in polyethylene upon exposure to TMA/ $\text{H}_2\text{O}$  ALD cycles. In addition, TMA exposure to C-10 alkane ( $(\text{CH}_2)_{10}-\text{COOH}$ ) self-assembled monolayers on silicon<sup>39</sup> also produced derivative-shaped features at 1467  $\text{cm}^{-1}$  which could also be ascribed to  $\text{CH}_2$  mode shifts upon reversible TMA penetration into the monolayer. The oscillations in mode intensity, with little change in chemical structure observed in the IR data after one TMA/ $\text{H}_2\text{O}$  exposure cycle, further indicate minimal chemical interaction between polypropylene and TMA.

Exposing PVA and PA-6 fibers and films to TMA resulted in significant changes in the IR spectra consistent with reaction. Fig. 7a shows *in situ* FTIR differential spectra collected during two ALD  $\text{Al}_2\text{O}_3$  cycles on PVA electrospun nanofibers at 90 °C. The spectra of the virgin PVA electrospun nanofibers and the absorbance scale bars are also shown. Characteristic modes<sup>37</sup> associated with PVA include a large associated O–H stretch at 3380  $\text{cm}^{-1}$ ,  $\text{CH}_2$  asymmetric stretch at 2910  $\text{cm}^{-1}$ , and C=O stretch at 1736  $\text{cm}^{-1}$  due to the presence of acetate groups. Modes between 1500 and 1100  $\text{cm}^{-1}$  include  $\text{CH}_2$  and O–H deformation at 1435  $\text{cm}^{-1}$ ,  $\text{CH}_3$  symmetric deformation at 1374  $\text{cm}^{-1}$ , C–O (acetate) stretching at 1246  $\text{cm}^{-1}$  and C–O (alcohol) stretching at 1096  $\text{cm}^{-1}$ . Upon TMA exposure, negative-going features correspond to decrease in O–H stretching, C=O stretching, O–H bending, and acetate-related C–O stretching modes at 1246  $\text{cm}^{-1}$ . These changes are consistent with TMA reacting with O–H and C=O bonding units. Similar to the PP case, new modes appear at 1200 and 700  $\text{cm}^{-1}$  indicating the presence of Al– $\text{CH}_3$ . The Al– $\text{CH}_3$  rocking mode expected near 1437  $\text{cm}^{-1}$  is obscured by the O–H bending feature. A derivative-shaped feature is also observed in the C–H<sub>2</sub> stretching region near 2929  $\text{cm}^{-1}$ . This is again consistent with TMA interacting with the polymer producing a blue shift in C–H vibrations. Any changes in the C–H<sub>2</sub> bending region near 1450  $\text{cm}^{-1}$  are hidden by the relatively larger changes in the O–H bending modes. Water exposure led to a small increase in –OH features and a decrease in Al– $\text{CH}_3$  group intensities near 1200 and 700  $\text{cm}^{-1}$ . The water also appears to remove C–H<sub>2</sub> stretching modes, as opposed to the reversible change observed in PP, again consistent with reaction between PVA and TMA. Changes in the acetate impurity features near 1736  $\text{cm}^{-1}$  are also noted. Repeating the TMA/ $\text{H}_2\text{O}$  cycle produced similar changes with smaller changes in intensity. The significant decrease in OH related absorbance upon the first TMA exposure is consistent with the large initial mass uptake

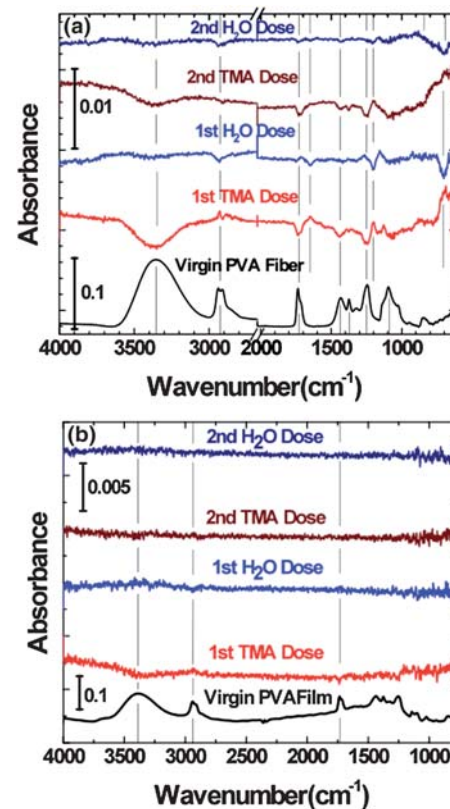


**Fig. 7** Absorbance and *in situ* differential FTIR spectra for untreated and coated PVA fibers (panel a) and PVA film (panel b). The differential spectra were collected during the first two  $\text{Al}_2\text{O}_3$  ALD cycles at 90 °C. Features of interest include: OH stretching (3380  $\text{cm}^{-1}$ ),  $\text{CH}_2$  stretching (2910  $\text{cm}^{-1}$ ), C=O stretching (1736  $\text{cm}^{-1}$ ),  $\text{CH}_3$  bending (1200  $\text{cm}^{-1}$ ),  $\text{CH}_3$  rocking (700  $\text{cm}^{-1}$ ). The absorbance for the differential spectra is magnified relative to the starting polymer absorbance, as indicated by the absorbance scale bars. The reduction in the hydroxyl peak demonstrates chemical interaction between the TMA and PVA.

observed with *in situ* QCM in Fig. 4a. Minimal reactivity upon water exposure indicates that the TMA reacts nearly completely in the previous step with surface hydroxyl groups. This is also consistent with the QCM data in Fig. 4a that show minimal mass uptake after water exposure during the first ALD cycle on PVA.

Fig. 7b shows *in situ* FTIR results collected at 90 °C after similar TMA and water exposures on a 30 nm thick planar PVA film cast onto a high resistivity silicon substrate. The spectra of the virgin PVA film and the absorbance scale bars are also shown. The spectra show the same characteristic modes as the PVA fibers. Upon the first TMA exposure, data in Fig. 7b show a decrease in the –OH signal intensity, but as expected for the smaller surface area available on a film relative to a fiber, the sensitivity to changes in mode signal is significantly reduced compared to the fiber substrates.

A silicon wafer coated with a ~30 nm thick PA-6 film was also exposed to  $\text{Al}_2\text{O}_3$  ALD cycles at 90 °C and characterized by FTIR. The resulting differential absorbance spectra are shown in Fig. 8. The absorbance of an uncoated PA-6 film shows characteristic peaks associated with hydrogen bonded N–H stretching at 3304  $\text{cm}^{-1}$ , the C–H<sub>2</sub> asymmetric and symmetric stretching features at 2930 and 2860  $\text{cm}^{-1}$ , and the amide I (C=O stretch)

feature at  $1640\text{ cm}^{-1}$ . The amide II (N–H bend/C–N stretch) and amide III (N=C=O skeletal vibration) bands are also present at  $1541\text{ cm}^{-1}$  and  $1280\text{ cm}^{-1}$ , respectively.<sup>40</sup> Exposing the PA-6 film to TMA produced significant changes in the IR modes, showing TMA is much more reactive with PA-6 than it is with PVA and PP. This is consistent with the large mass uptake during TMA exposure to the PA-6, as shown in the QCM results in Fig. 4. Upon TMA exposure, the N–H feature at  $3304\text{ cm}^{-1}$  and amide I feature at  $1640\text{ cm}^{-1}$  decreased in intensity. The TMA exposure also affected the C–H stretching modes and produced visible methyl rocking and deformation modes at  $1437\text{ cm}^{-1}$ ,  $1190\text{ cm}^{-1}$  and  $690\text{ cm}^{-1}$ . Changes are also noted when the TMA-exposed sample is subsequently exposed to  $\text{H}_2\text{O}$ . Water exposure removed the Al–CH<sub>3</sub> features and produced an increase in Al–O stretching modes in the  $\sim 700\text{ cm}^{-1}$  range. Interestingly, the N–H stretching mode increased after water exposure. The removal of the methyl groups and increase in Al–O are consistent with water reacting with Al–CH<sub>3</sub> groups.

The IR data in Fig. 8 clearly indicate a reaction involving the TMA and the carbonyl group present in the PA-6. The data are consistent with the reaction following a Grignard mechanism, in which the TMA attacks the electrophilic carbon atom in the carbonyl group to produce C–O–Al– and C–CH<sub>3</sub> bonding groups through methyl insertion from the TMA. Also, the reduction of the N–H stretching mode at  $3290\text{ cm}^{-1}$  demonstrates interaction with the secondary amine group. Previous *ab initio* studies<sup>41</sup> suggest that reactions between TMA and primary amine terminal groups on self-assembled monolayers are kinetically unfavorable at low temperatures. The decrease in N–H mode intensity could result from reaction between N–H and TMA, where the hydrogen bonded environment of the secondary amine group in PA-6, which is not present in the surface terminated SAM, can help to enhance the kinetics at lower

temperatures. The reaction could involve insertion of TMA into the hydrogen bonded NH–O=C unit to produce Al–N bonding and CH<sub>4</sub>. The water exposure step also produces an apparent increase in N–H mode intensity. Hydrogen bonding places the hydrogen in a much more polar environment, increasing the intensity of the associated vibrational modes.<sup>42</sup> Therefore, we assign the increase in N–H intensity upon water exposure to a transition from isolated to hydrogen bonded N–H groups that occurs upon oxygen incorporation.

#### D. TEM analysis of TMA/water exposure on polymer fibers

Cross-sectional transmission electron microscope images of PP and PA-6 fibers coated with ALD Al<sub>2</sub>O<sub>3</sub> are shown in Fig. 9 and 10. Fig. 9a and b display TEM images of PP fibers after exposure to 100 cycles of ALD Al<sub>2</sub>O<sub>3</sub> at  $60^\circ\text{C}$  and  $90^\circ\text{C}$ , respectively. The deposition at higher temperature produces more net inorganic material on or near the fiber surface (contrast extends over nearly  $100\text{ nm}$  after 100 ALD cycles at  $90^\circ\text{C}$ ) as compared to the lower temperature deposition (TEM contrast extends  $<50\text{ nm}$ ). This result is consistent with the larger mass uptake observed over 25 ALD cycles at  $90^\circ\text{C}$  compared to  $60^\circ\text{C}$  in the data in Fig. 5a. The non-uniform deposition observed in the TEM images, especially under higher temperature conditions, is ascribed to precursor diffusion and reaction into the near-surface region of the polymer fiber. Similar results are observed upon Al<sub>2</sub>O<sub>3</sub> ALD at  $125^\circ\text{C}$  onto poly-3-hexyltiophene (P3HT) and poly-vinyl-phenol (PVP).<sup>20</sup> A diffuse and rough interface is observed for films deposited on P3HT, which is not expected to have any chemical interaction with TMA, but an abrupt interface was observed on the more reactive PVP.

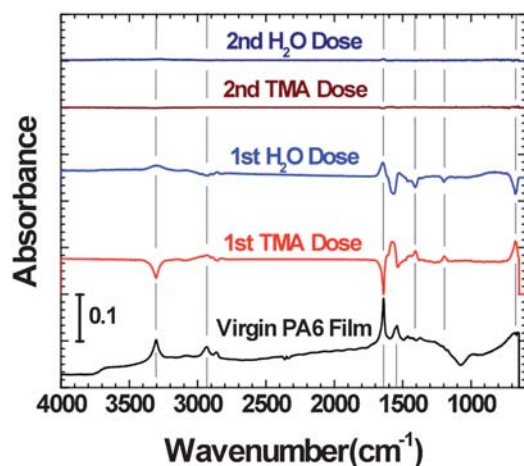


**Fig. 8** Absorbance spectrum for an  $\sim 30\text{ nm}$  thick uncoated PA-6 film, and *in situ* differential FTIR spectra collected during two ALD cycles at  $90^\circ\text{C}$ . The absorbance scale is the same for all spectra. The spectra show hydrogen bonded NH stretching ( $3304\text{ cm}^{-1}$ ), CH<sub>2</sub> stretching ( $2930\text{ cm}^{-1}$ ), amide I (CO stretching) ( $1640\text{ cm}^{-1}$ ), C–H stretching (2860–2930 cm<sup>-1</sup>), CH<sub>3</sub> bending ( $1437\text{ cm}^{-1}$ ,  $1190\text{ cm}^{-1}$ ) and CH<sub>3</sub> rocking ( $690\text{ cm}^{-1}$ ). The large signal strength is consistent with a larger extent of reaction between PA-6 and TMA during the first ALD cycle compared to the other polymers studied.

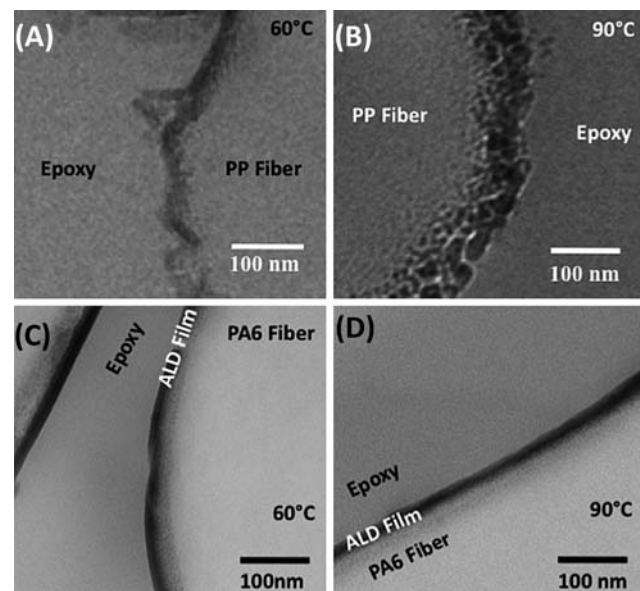


**Fig. 9** Cross-sectional transmission electron micrographs of PP (A and B) and PA-6 fibers (C and D) exposed to 100 ALD Al<sub>2</sub>O<sub>3</sub> cycles at  $60^\circ\text{C}$  (A and C) and  $90^\circ\text{C}$  (B and D). For deposition on polypropylene, the structure of the deposited material depends significantly on deposition temperature between  $60$  and  $90^\circ\text{C}$ , whereas for deposition on PA-6, similar structure is observed after deposition at the two temperatures.

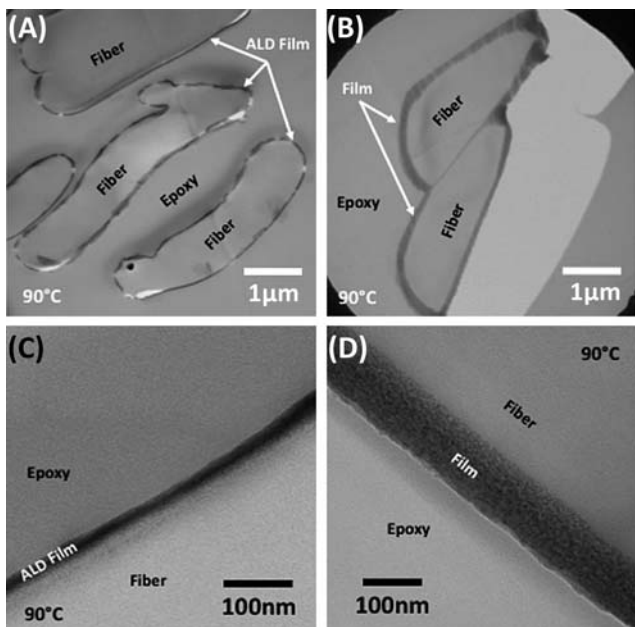


**Fig. 10** TEM of cross-sections prepared by microtome, of PA-6 fibers exposed to the ALD process (A and C), and similar fibers after prolonged TMA precursor soaks (B and D). A thicker layer with a more diffuse interface is observed in the sample subjected to extended precursor exposure.

Typical PA-6 fibers coated with 100 ALD  $\text{Al}_2\text{O}_3$  cycles at 60 and 90 °C were imaged by TEM, and results are shown in Fig. 9c and d. The deposition on PA-6 results in a more continuous  $\text{Al}_2\text{O}_3$  film at both temperatures. However, at both 60 and 90 °C deposition, image contrast is observed in the fiber region close to the film coating, also suggesting precursor diffusion and penetration into the fiber.

The QCM and IR results indicate that significant reaction between the PA-6 and the TMA occurs very early (during the first cycle) in the ALD process. We therefore performed experiments to examine effects of a single TMA exposure on the structure of PA-6 fibers. Fig. 10, panels a and c, presents cross-sectional TEM images at two levels of magnification of PA-6 fibers coated with 100 ALD  $\text{Al}_2\text{O}_3$  cycles at 90 °C. They show that 100 cycles at 90 °C result in a uniform coating ~20 nm thick on the surface. Fig. 10, panels b and d, provide images of PA-6 fibers subjected to extended TMA exposures (60 sequential steps of 1 minute each) followed by extended water exposures (20 steps of 1 minute each). These images show that long exposures result in a thicker but less dense layer on the fiber surface. The high magnification image in panel d shows the layer to be ~100 nm thick, with mottled structure and non-uniform contrast. The extended TMA exposures result in significant reaction in the fiber near-surface region, and that the chemical composition is modified to a depth of 100 nm or more.

#### E. Comparison with other studies

The  $\text{Al}_2\text{O}_3$  film nucleation and growth behavior are expected to depend on the chemical nature of the polymer substrate.<sup>11,20,41</sup> Wilson *et al.* observed trends in mass uptake during TMA exposure at 85 °C to nonreactive polymers<sup>11</sup> including polypropylene,

poly(methyl methacrylate) (PMMA), polyethylene (PE), poly(vinyl chloride) (PVC) and polystyrene (PS). They found that precursor permeability generally scaled with expected trends in precursor solubility and diffusivity within the polymer matrix. The results shown here for the nonreactive polypropylene follow similar results, with some quantitative distinctions. The data we show in Fig. 4 for ALD on PP display a significantly smaller mass gain upon TMA exposure compared to that shown by Wilson *et al.* under similar ALD conditions. This difference could be due to the thicker film used by Wilson *et al.*, (200 nm versus 30 nm used here) where a thicker film is expected to absorb a larger precursor mass. The difference in mass uptake could also be due to differences in the molecular weight, tacticity or degree of crystallinity of the polypropylene used. The observed temperature dependence of precursor diffusion, displayed in Fig. 5 and 9, shows enhanced precursor permeability with increasing temperature, consistent with increased diffusivity upon polymer thermal expansion. Earlier studies of ALD  $\text{Al}_2\text{O}_3$  water penetration barriers on poly(ether sulfone) suggest that higher deposition temperatures improve barrier performance,<sup>43</sup> whereas other studies of plasma assisted ALD  $\text{Al}_2\text{O}_3$  water barriers on poly(2,6-ethyl-phenenaphthalate) indicate improved performance at lower temperatures.<sup>44</sup> While barrier properties of our materials were not measured, the mass uptake and TEM results shown here suggest that lower deposition temperatures will decrease precursor penetration and produce more cohesive coatings on nonreactive polymer substrates.

Many polymer systems offer reactive sites for interaction with TMA and other ALD precursors. We find that PVA (with reactive  $-OH$  units) and PA-6 (with amide bonding units,  $HNC=O$ ) show much higher TMA uptake compared to the more nonreactive polypropylene. Also, reactions are not limited to the polymer surface, and significant precursor penetration and near-surface reaction can proceed. The more reactive polymers show an extent of reaction that is also dependent on substrate temperature, although results show significant TMA diffusion and reaction in polyamide-6 at 60 and 90 °C. In general, therefore, to control ALD film growth on polymer substrates, one must consider and balance mechanisms associated with precursor dissolution, diffusion, and reaction with the polymer of interest.

#### IV. Summary and conclusions

Results demonstrate that initial reactions during vapor-phase metal-organic precursor exposure on polymers depend strongly on the polymer substituents and degrees of chain association of the polymer units. Polypropylene, with  $-\text{CH}_3$  groups, shows nonreactive adsorption of TMA, whereas polyamide-6 with reactive amide bonding units undergoes rapid reaction with trimethylaluminium, producing a large mass uptake during the first TMA exposure cycle. FTIR results suggest that TMA can insert into the amide bond unit, following a Grignard reaction, resulting in methyl group insertion and formation of  $-\text{C}-\text{O}-\text{Al}-$  bonds. The IR data show that the secondary amine group present in the PA-6 is also affected by TMA exposure. We propose that the TMA reacts with the NH in PA-6 because of rate enhancement by the  $\text{NH}\cdots\text{O}=\text{C}$  hydrogen bond, and/or the TMA/carbonyl reaction displaces the hydrogen bond which reduces the intensity of the N-H stretch observed by IR. Subsequent oxidation then

allows the hydrogen bond to reform, increasing the N–H stretching absorbance. Polyvinyl alcohol films and fibers also show enhanced reactivity with TMA during early ALD cycles, relative to PP, with FTIR results indicating interaction between TMA and PVA's hydroxyl functional groups. Polypropylene shows mass uptake at 60 °C similar to that measured during Al<sub>2</sub>O<sub>3</sub> ALD on dense Al<sub>2</sub>O<sub>3</sub> substrates. At 90 °C, a larger mass uptake is observed consistent with enhanced precursor diffusion. More extensive precursor penetration is expected in polymers with few reactive sites such as polypropylene. The FTIR analysis during TMA exposure to polypropylene shows shifting of the CH<sub>2</sub> band frequencies, but little chemical interaction between the polypropylene and TMA, consistent with the QCM measurements. This improved understanding of specific precursor/polymer interaction processes could be important to improve and optimize the quality of low temperature inorganic passivation layers and other coatings on polymer films and fibers.

## Acknowledgements

Support for this work is acknowledged from the Nonwovens Cooperative Research Center at North Carolina State University (NCRC) Project 07-105, NSF project STTR #0740487, NSF CBET #0626256, and DOE project #08NT0001925. The authors acknowledge Profs. C. B. Gorman and B. M. Novak for helpful discussions.

## References

- J. S. Lewis and M. S. Weaver, Thin-film permeation-barrier technology for flexible organic light-emitting devices, *IEEE J. Sel. Top. Quantum Electron.*, 2004, **10**(1), 45–57.
- H. Chatham, Oxygen diffusion barrier properties of transparent oxide coatings on polymeric substrates, *Surf. Coat. Technol.*, 1996, **78**(1–3), 1–9.
- P. W. Gibson, H. L. Schreuder-Gibson and D. Rivin, Electrospun fiber mats: transport properties, *AIChE J.*, 1999, **45**(1), 190–195.
- C. Burger, B. S. Hsiao and B. Chu, Nanofibrous materials and their applications, *Annu. Rev. Mater. Res.*, 2006, **36**, 333–368.
- G. K. Hyde, S. D. McCullen, S. Jeon, S. M. Stewart, H. Jeon, E. G. Loba and G. N. Parsons, Atomic layer deposition and biocompatibility of titanium nitride nano-coatings on cellulose fiber substrates, *Biomed. Mater. (Bristol, U. K.)*, 2009, **4**(2), 025001.
- Z. W. Ma, M. Kotaki, R. Inai and S. Ramakrishna, Potential of nanofiber matrix as tissue-engineering scaffolds, *Tissue Eng.*, 2005, **11**(1–2), 101–109.
- J. C. Rotger, J. J. Pireaux, R. Caudano, N. A. Thorne, H. M. Dunlop and M. Bennalek, Deposition of silicon-oxide onto polyethylene and polyethyleneterephthalate—an X-ray photoelectron-spectroscopy interfacial study, *J. Vac. Sci. Technol. A*, 1995, **13**(2), 260–267.
- R. Cueff, G. Baud, M. Bennalek, J. P. Besse, J. R. Butruille and M. Jacquet, X-Ray photoelectron spectroscopy studies of plasma-modified PET surface and alumina/PET interface, *Appl. Surf. Sci.*, 1997, **115**(3), 292–298.
- A. Hooper, G. L. Fisher, K. Konstadinidis, D. Jung, H. Nguyen, R. Opila, R. W. Collins, N. Winograd and D. L. Allara, Chemical effects of methyl and methyl ester groups on the nucleation and growth of vapor-deposited aluminum films, *J. Am. Chem. Soc.*, 1999, **121**(35), 8052–8064.
- Y. Lettier, Durability of nanosized oxygen-barrier coatings on polymers, *Prog. Mater. Sci.*, 2003, **48**, 1–55.
- C. A. Wilson, R. K. Grubbs and S. M. George, Nucleation and growth during Al<sub>2</sub>O<sub>3</sub> atomic layer deposition on polymers, *Chem. Mater.*, 2005, **17**(23), 5625–5634.
- N. L. Jeon, R. G. Nuzzo, Y. N. Xia, M. Mrksich and G. M. Whitesides, Patterned self-assembled monolayers formed by microcontact printing direct selective metalization by chemical-vapor-deposition on planar and nonplanar substrates, *Langmuir*, 1995, **11**(8), 3024–3026.
- R. Chen, H. Kim, P. C. McIntyre and S. F. Bent, Investigation of self-assembled monolayer resists for hafnium dioxide atomic layer deposition, *Chem. Mater.*, 2005, **17**(3), 536–544.
- K. J. Park, J. M. Doub, T. Gougois and G. N. Parsons, Microcontact patterning of ruthenium gate electrodes by selective area atomic layer deposition, *Appl. Phys. Lett.*, 2005, **86**(5), 051903.
- E. Farm, M. Kemell, E. Santala, M. Ritala and M. Leskela, Selective-area atomic layer deposition using poly(vinyl pyrrolidone) as a passivation layer, *J. Electrochem. Soc.*, 2010, **157**(1), K10–K14.
- A. S. D. Sobrinho, M. Latreche, G. Czeremuszkin, J. E. Klemburg-Sapieha and M. R. Wertheimer, Transparent barrier coatings on polyethylene terephthalate by single- and dual-frequency plasma-enhanced chemical vapor deposition, *J. Vac. Sci. Technol. A*, 1998, **16**(6), 3190–3198.
- R. Morent, N. De Geyter, J. Verschuren, K. De Clerck, P. Kiekens and C. Leys, Non-thermal plasma treatment of textiles, *Surf. Coat. Technol.*, 2008, **202**(14), 3427–3449.
- J. D. Ferguson, A. W. Weimer and S. M. George, Atomic layer deposition of Al<sub>2</sub>O<sub>3</sub> films on polyethylene particles, *Chem. Mater.*, 2004, **16**(26), 5602–5609.
- M. D. Groner, S. M. George, R. S. McLean and P. F. Garcia, Gas diffusion barriers on polymers using Al<sub>2</sub>O<sub>3</sub> atomic layer deposition, *Appl. Phys. Lett.*, 2006, **88**(5), 051907.
- S. Ferrari, F. Perissinotti, E. Peron, L. Fumagalli, D. Natali and M. Sampietro, Atomic layer deposited Al<sub>2</sub>O<sub>3</sub> as a capping layer for polymer based transistors, *Org. Electron.*, 2007, **8**(4), 407–414.
- C. A. Wilson, J. A. McCormick, A. S. Cavanagh, D. N. Goldstein, A. W. Weimer and S. M. George, Tungsten atomic layer deposition on polymers, *Thin Solid Films*, 2008, **516**(18), 6175–6185.
- R. Cooper, H. P. Upadhyaya, T. K. Minton, M. R. Berman, X. H. Du and S. M. George, Protection of polymer from atomic-oxygen erosion using Al<sub>2</sub>O<sub>3</sub> atomic layer deposition coatings, *Thin Solid Films*, 2008, **516**(12), 4036–4039.
- A. A. Dameron, S. D. Davidson, B. B. Burton, P. F. Garcia, R. S. McLean and S. M. George, Gas diffusion barriers on polymers using multilayers fabricated by Al<sub>2</sub>O<sub>3</sub> and rapid SiO<sub>2</sub> atomic layer deposition, *J. Phys. Chem. C*, 2008, **112**(12), 4573–4580.
- J. Meyer, D. Schneidenbach, T. Winkler, S. Hamwi, T. Weimann, P. Hinze, S. Ammermann, H. H. Johannes, T. Riedl and W. Kowalsky, Reliable thin film encapsulation for organic light emitting diodes grown by low-temperature atomic layer deposition, *Appl. Phys. Lett.*, 2009, **94**(23), 233305.
- G. K. Hyde, G. Scarel, J. C. Spagnola, Q. Peng, K. Lee, B. Gong, K. G. Roberts, K. M. Roth, C. A. Hanson, C. K. Devine, S. M. Stewart, D. Hojo, J.-S. Na, J. S. Jur and G. N. Parsons, Atomic layer deposition and abrupt wetting transitions on nonwoven polypropylene and woven cotton fabrics, *Langmuir*, 2010, **26**(4), 2550–2558.
- J. S. Jur, J. C. Spagnola, K. Lee, B. Gong, Q. Peng and G. N. Parsons, Temperature-dependent sub-surface growth during atomic layer deposition on polypropylene and cellulose fibers, *Langmuir*, 2010, DOI: 10.1021/la904604z.
- M. Leskela, M. Kemell, K. Kukli, V. Pore, E. Santala, M. Ritala and J. Lu, Exploitation of atomic layer deposition for nanostructured materials, *Mater. Sci. Eng., C*, 2007, **27**, 1504–1508.
- Q. Peng, X. Y. Sun, J. C. Spagnola, G. K. Hyde, R. J. Spontak and G. N. Parsons, Atomic layer deposition on electrospun polymer fibers as a direct route to Al<sub>2</sub>O<sub>3</sub> microtubes with precise wall thickness control, *Nano Lett.*, 2007, **7**(3), 719–722.
- G. M. Kim, S. M. Lee, G. H. Michler, H. Roggendorf, U. Gosele and M. Knez, Nanostructured pure anatase titania tubes replicated from electrospun polymer fiber templates by atomic layer deposition, *Chem. Mater.*, 2008, **20**(9), 3085–3091.
- M. Kemell, M. Ritala, M. Leskela, R. Groenen and S. Lindfors, Coating of highly porous fiber matrices by atomic layer deposition, *Chem. Vap. Deposition*, 2008, **14**(11–12), 347–352.
- T. J. Stark, G. M. Shedd, J. Vitarelli, D. P. Griffis and P. E. Russell, H<sub>2</sub>O enhanced focused ion beam micromachining, *J. Vac. Sci. Technol. B*, 1995, **13**(6), 2565–2569.
- J. W. Elam, M. D. Groner and S. M. George, Viscous flow reactor with quartz crystal microbalance for thin film growth by atomic layer deposition, *Rev. Sci. Instrum.*, 2002, **73**(8), 2981–2987.
- M. D. Groner, F. H. Fabreguette, J. W. Elam and S. M. George, Low-temperature Al<sub>2</sub>O<sub>3</sub> atomic layer deposition, *Chem. Mater.*, 2004, **16**(4), 639–645.

- 34 J. S. Na, Q. Peng, G. Scarel and G. N. Parsons, Role of gas doping sequence in surface reactions and dopant incorporation during atomic layer deposition of Al-doped ZnO, *Chem. Mater.*, 2009, **21**(23), 5585–5593.
- 35 A. C. Dillon, A. W. Ott, J. D. Way and S. M. George, Surface chemistry of  $\text{Al}_2\text{O}_3$  deposition using  $\text{Al}(\text{CH}_3)_3$  and  $\text{H}_2\text{O}$  in a binary reaction sequence, *Surf. Sci.*, 1995, **322**(1–3), 230–242.
- 36 L. Vlaev, D. Damyanov and M. M. Mohamed, Infrared spectroscopy study of the nature and reactivity of a hydrate coverage on the surface of  $\gamma\text{-Al}_2\text{O}_3$ , *Colloids Surf.*, 1989, **36**(3), 427–437.
- 37 I. Noda, A. E. Dowrey, J. L. Haynes and C. Marcott, Group frequency assignments for major infrared bands observed in common synthetic polymers, in *Physical Properties of Polymers Handbook*, ed. J. E. Mark, Springer, New York, 2007.
- 38 T. R. Gow, R. Lin, L. A. Cadwell, F. Lee, A. L. Backman and R. I. Masel, Decomposition of trimethylaluminum on silicon(100), *Chem. Mater.*, 1989, **1**, 406–411.
- 39 M. Li, M. Dai and Y. J. Chabal, Atomic layer deposition of aluminum oxide on carboxylic acid-terminated self-assembled monolayers, *Langmuir*, 2009, **25**(4), 1911–1914.
- 40 W. F. Maddams, Infared and Raman spectroscopy, in *Analysis of Polymer Systems*, ed. L. S. Bark and N. S. Allen, Applied Science Publishers, London, 1982.
- 41 Y. Xu and C. B. Musgrave, A DFT study of the  $\text{Al}_2\text{O}_3$  atomic layer deposition on SAMs: effect of SAM termination, *Chem. Mater.*, 2004, **16**(4), 646–653.
- 42 W. O. George and D. J. McIntyre, *Infrared Spectroscopy*, John Wiley & Sons, New York, 1987, p. 458.
- 43 S. H. K. Park, J. Oh, C. S. Hwang, J. I. Lee, Y. S. Yang and H. Y. Chu, Ultrathin film encapsulation of an OLED by ALD, *Electrochem. Solid-State Lett.*, 2005, **8**(2), H21–H23.
- 44 E. Langereis, M. Creatore, S. B. S. Heil, M. C. M. Van de Sanden and W. M. M. Kessels, Plasma-assisted atomic layer deposition of  $\text{Al}_2\text{O}_3$  moisture permeation barriers on polymers, *Appl. Phys. Lett.*, 2006, **89**(8), 081915.